sustainability

MDPI

Article

Acoustic Emission Characteristics of the Water Weakening Effect on Cretaceous Weakly Cemented Sandstone

Yuru Yang [1], Wenping Li [1,*] and Qinggang Lu [2]

[1] School of Resources and Geosciences, China University of Mining and Technology, Xuzhou 221116, China
[2] State Investment Hami Energy Development Co., Ltd., Hami 839000, China
* Correspondence: liwp@cumt.edu.cn

Abstract: Rock mass stability is often affected by water–rock interaction in underground engineering construction. Cretaceous sandstones often have weak cementation, low strength and strong water-holding capacity, and their rock mass strength is easily weakened by these activities. In this paper, the uniaxial compressive strength (UCS) and tensile strength (TS) of weakly cemented Cretaceous sandstones from different sedimentary facies under natural and saturated conditions were tested, and the loading process was monitored by the acoustic emission (AE) technique. The results show that the existence of water obviously weakened the mechanical properties of weakly cemented sandstone. The UCS and TS of saturated braided river facies sandstone decreased to 41.24% and 35.95% of their natural states, respectively, while those of desert facies sandstone decreased to 32.90% and 26.98% of their natural states, respectively. The AE characteristics of sandstone from different sedimentary facies were similar during loading due to weakening by water, including a decrease in cumulative AE energy, b-value fluctuation and reduction in the peak frequency distribution range. Fracture in the Brazilian splitting test was mainly due to the rapid initiation and coalescence of microcracks near the peak point. However, in the uniaxial compression test, the macro fractures were caused by many microcracks that occurred continuously during loading and finally connected. The high quartz and low feldspar contents strengthened the mechanical properties of braided fluvial facies sandstone compared to those of desert facies sandstone and lessened the effect of water weakening.

Keywords: Cretaceous sandstone; AE characteristics; mechanical properties; sedimentary facies; water weakening

check for updates

Citation: Yang, Y.; Li, W.; Lu, Q. Acoustic Emission Characteristics of the Water Weakening Effect on Cretaceous Weakly Cemented Sandstone. *Sustainability* **2023**, *15*, 8390. https://doi.org/10.3390/su15108390

Academic Editor: Fernando António Leal Pacheco

Received: 30 March 2023
Revised: 15 May 2023
Accepted: 15 May 2023
Published: 22 May 2023

Copyright: © 2023 by the authors. Licensee MDPI, Basel, Switzerland. This article is an open access article distributed under the terms and conditions of the Creative Commons Attribution (CC BY) license (https://creativecommons.org/licenses/by/4.0/).

1. Introduction

The presence of groundwater greatly weakens the strength of rock masses in practical engineering applications, such as slope engineering [1], underground openings [2,3] and dam foundation stability [4]. Many scholars have studied water–rock interactions and the influence of water on the mechanical properties of rock [5–7]. It has been found that the degree to which rocks with different lithologies are weakened is different. The uniaxial compressive strength (UCS) of saturated limestone collected from southern Iran was 70% of that in the dried state [8]. The UCS of Gosford sandstone was only 30% of that of "completely" dry samples [9]. Even for nearly impermeable crystalline rock, water reduced the strength of the rock to 80% of that in the dry state [10].

When rock is deformed or damaged by force, it releases energy in the form of elastic waves, which is the acoustic emission (AE) phenomenon [11]. The AE monitoring instrument that uses this phenomenon to monitor the damage and failure process of rock and locate the positions of microcracks has been developed [12]. This technique is the most convenient and efficient way to realize real-time monitoring of rock failure without external force damage. Many types of AE characteristics can be used to study the damage process in rocks. For example, Ge and Sun [13] analyzed the variation in *b*-value characteristics in granite under stress after heating and cooling cycles; Han et al. [14] discovered the change

in the AE signal intensity as well as the AF (average frequency) versus RA (rise time divided by the amplitude) in concrete beam bending tests; Shi et al. [15] observed the spatial characteristics of AE events during uniaxial compression creep in fine sandstone; Geng and Cao [16] researched the cumulative AE energy change in water-bearing sandstone during loading. In addition, other specific characteristics including AE counts, amplitude, rise time, hits and frequency are used in AE signal analysis [17,18].

Weakly cemented sandstone is the host rock in Cretaceous strata which is widely distributed in Northwest China. Due to the influence of tectonic activities, sandstones in the same area may have different sedimentary facies with different properties. Due to its short period of diagenesis, the mineral grain cementation is poor, and the textural components and textural maturity are low. The cementation of the sandstone is weak, so the strength is low, and it is easily disturbed. It has a strong water-bearing capacity, and is easy to hydrolyze and weather [19,20]. In recent years, as engineering activities have increased, studies of weakly cemented sandstone have been carried out [20–22], but the effect of water on the mechanical properties of these weakly cemented sandstones is not clear. In this paper, two typical Cretaceous weakly cemented sandstones with different sedimentary facies were collected from the Ordos Basin, China. Brazilian splitting tests and uniaxial compression tests were carried out to study the weakening effect of water on the mechanical properties of these sandstones. AE equipment was used to monitor the failure process, and the variations in AE energy, the *b*-value, the peak frequency and the spatial location of natural and saturated samples were compared. This study can provide guidance for understanding the influence of water on the mechanical behavior of weakly cemented Cretaceous sandstone.

2. Methodology

2.1. Sample Preparation

The sandstones were collected from the Cretaceous Luohe Formation in the Ordos Basin, China, and included braided fluvial and desert facies; the specific information about the sandstone was provided in our previous literature [23,24]. To eliminate the interference of irrelevant factors, fine sandstone without obvious bedding was selected. The average densities of braided fluvial facies and the desert facies sandstones were 2.195 g/cm^3 and 2.062 g/cm^3, respectively.

According to the method proposed by the International Society for Rock Mechanics (ISRM) [25], the samples with height-to-diameter ratios of 2 and 0.5 were selected for the uniaxial compressive test and Brazilian test, respectively. The rock samples were processed into cylinders of ϕ 50 mm × 100 mm and discs of ϕ 50 mm × 25 mm. Before the tests, the wave velocities of all samples were determined to ensure homogeneity. Both the disc and cylinder samples were divided into two groups. The natural moisture content (average of approximately 1.22% for the braided fluvial facies and 1.41% for the desert facies) of the first group was maintained. To remove adhesive water, the other group was dried in an oven at 50 °C until the mass almost ceased to change. Then, these dry samples were soaked in purified water. The mass was measured every 10 min at the beginning, and as the water absorption rate slowed down, the mass was measured every 4 h until changes no longer occurred. Figure 1 shows that the braided fluvial facies sandstone reached saturation, with an average relative water content of 4.15% after 20 h, and the desert facies sandstone reached a saturation of 5.62% after 60 h. Table 1 summarizes the physical parameters and dimensions of the samples used in this study.

2.2. Test Equipment and Procedure

The test equipment included a rock mechanics loading system and an AE acquisition system. The uniaxial compression and Brazilian splitting tests were completed using a WES-D1000 computer-controlled hydraulic universal testing machine, which was equipped with high-precision sensors on the pressure head and could automatically record the load, time, displacement and other data. The displacement control loading method was used in

the tests, and the loading rate was set to 0.02 mm/s. The DS5-8B AE acquisition system produced by Beijing Softland Times Scientific and Technology Co., Ltd. (Beijing, China) was used to determine the AE properties of the samples during loading. This AE system can realize the acquisition of acoustic signals, spatial positioning of AE signals, AE event statistics and determination of event occurrence times. During the test, the AE signal was collected by the sensor, amplified by an amplifier, entered into the signal processing system and automatically recorded. The AE sensor used in this experiment is an RS-2A type sensor, with a diameter of 18.8 mm, a height of 15 mm, a frequency response range of 60–400 kHz and a center frequency of 150 kHz. A layer of Vaseline was applied to ensure sufficient coupling between the AE sensors and the sample, and then the sensors were fixed to the surface of the sample. As shown in Figure 2, six AE sensors were coupled at different positions on the sample to receive AE signals. By using the Geiger algorithm [13,16], the AE acquisition system retrieved the position of the AE signal source and located AE events automatically. Before testing, ambient noise was measured to avoid the influence of environmental noise. The threshold value and sampling frequency were set to 25 dB and 3 MHz, respectively. During the test, AE data were collected as soon as the testing machine was started and until the sample was damaged. After the test, all the collected data were processed and analyzed.

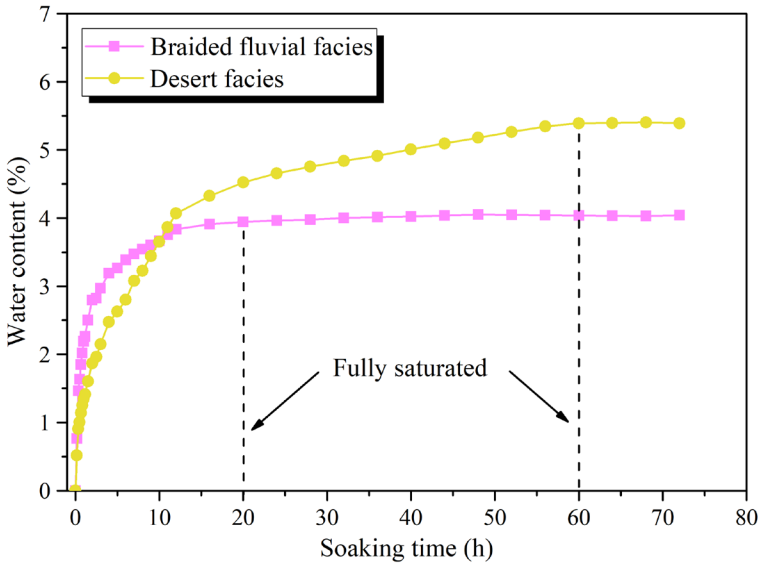


Figure 1. The variation in the water content of sandstone over time.

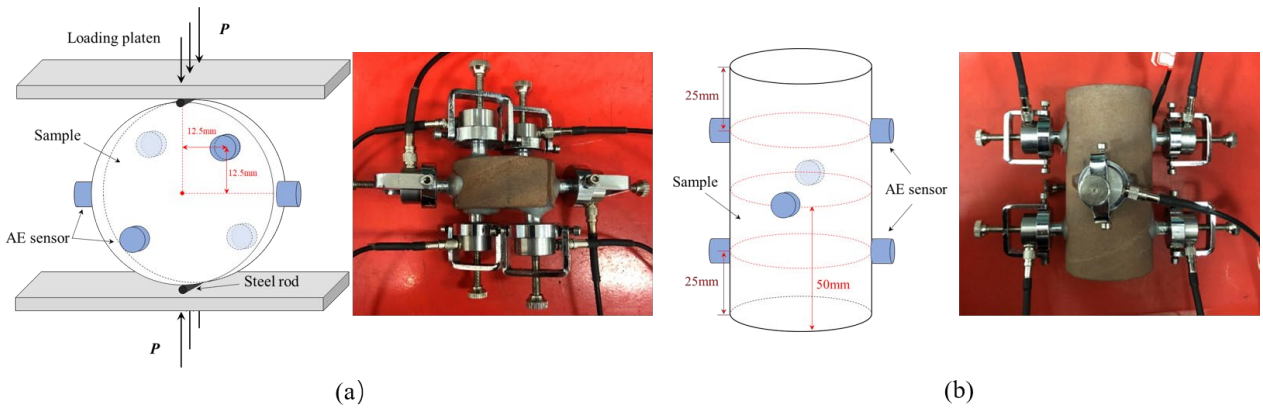


Figure 2. Location of AE sensors in the (**a**) Brazilian disc test and (**b**) uniaxial compressive test.

Table 1. Physical parameters and dimensions of samples.

No.	Sedimentary Facies	State	Water Contents (%)	Density (g/cm^3)	Diameter (mm)	Height (mm)	Strength (MPa)
B-BN-1	Braided fluvial facies	Natural	1.20	2.15	49.60	25.16	1.47
B-BN-2			1.25	2.19	49.56	25.27	1.32
B-BN-3			1.18	2.22	49.55	25.21	1.56
B-BS-1		Fully saturated	4.21	2.45	49.62	24.71	0.48
B-BS-2			4.26	2.39	49.17	24.38	0.53
B-BS-3			4.19	2.43	48.71	24.97	0.39
B-DN-1	Desert facies	Natural	1.39	2.16	49.18	25.13	1.11
B-DN-2			1.45	2.03	49.79	25.38	1.21
B-DN-3			1.48	2.09	49.67	24.65	1.05
B-DS-1		Fully saturated	5.68	2.36	49.49	24.45	0.3
B-DS-2			5.59	2.33	49.21	25.06	0.22
B-DS-3			5.65	2.29	49.68	25.22	0.35
C-BN-1	Braided fluvial facies	Natural	1.16	2.18	49.53	100.48	27.33
C-BN-2			1.23	2.17	49.38	99.88	26.71
C-BN-3			1.28	2.24	49.55	100.14	25.81
C-BS-1		Fully saturated	4.15	2.37	49.41	100.39	11.01
C-BS-2			4.07	2.43	49.58	100.15	10.12
C-BS-3			4.02	2.41	49.55	100.29	11.73
C-DN-1	Desert facies	Natural	1.47	2.14	49.01	100.16	23.47
C-DN-2			1.32	1.99	49.64	100.32	25.11
C-DN-3			1.34	2.07	49.56	100.40	22.93
C-DS-1		Fully saturated	5.53	2.29	49.19	100.23	8.45
C-DS-2			5.67	2.32	49.60	99.92	7.9
C-DS-3			5.62	2.26	49.27	100.29	8.88

3. Results

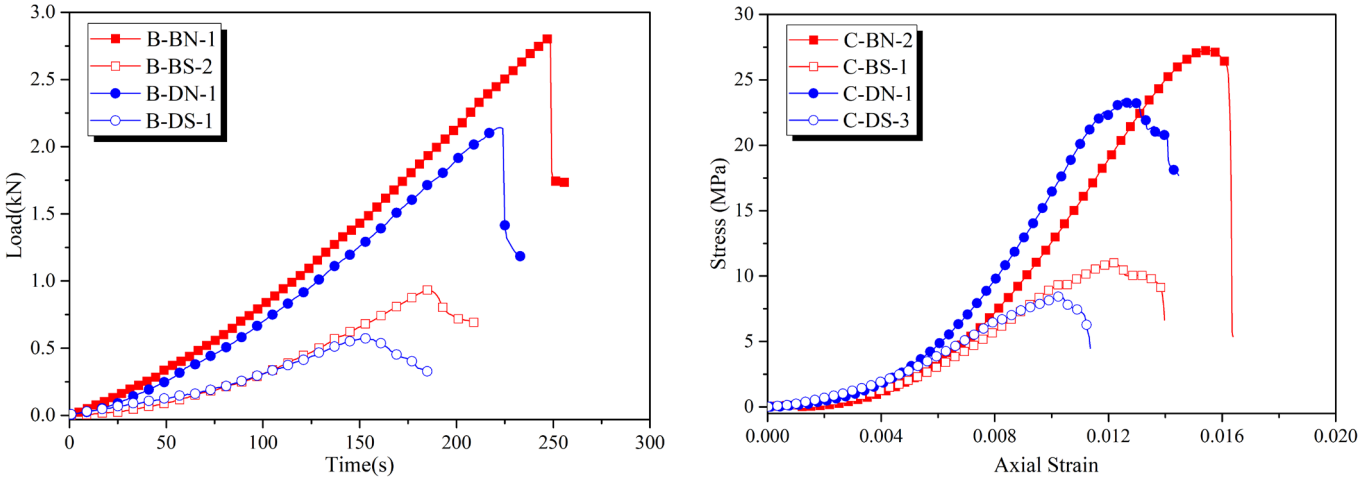
3.1. Effect of Water on Mechanical Properties

The whole test results were listed in Table 1. The median test results of each group were selected for comparison. Figure 3 shows the variations in the tensile and compressive strengths of the braided river and desert facies sandstone. In the Brazilian disk test (Figure 3a), the curve included three stages: initial compaction, linear evolution and rapid decrease after the peak [26]. The bearing capacity of sandstone in the natural state decreased rapidly with little change in axial strain when the axial load reached the peak value, showing brittle failure characteristics. As represented in Figure 3b, the stress–strain curve mainly included the stages of initial compaction, elastic deformation, yield segments and post-peak failure. The sandstone in its natural state showed brittle failure characteristics. However, under fully saturated conditions, the initial compaction stage of the uniaxial compression test was longer than that of natural sandstone, and the linear growth stage was shorter. After a short linear growth stage, the fully saturated sandstone entered the crack growth stage; when the axial load reached its peak, the decrease in bearing capacity of the sample was accompanied by significant axial strain, and the sample brittleness was not as obvious as in its natural state.

The TS was calculated using the following equation [25]:

$$\mathrm{TS} = \frac{2P}{\pi D t}, \tag{1}$$

where P is the peak load, in N; D is the diameter of the sample, in m; and t is the thickness of the sample measured at the center, in m.



(**a**) (**b**)

Figure 3. Effect of water on mechanical properties of sandstone: (**a**) Brazilian test; (**b**) uniaxial compressive test.

In the natural state, the UCS and TS of braided river facies sandstone were 26.71 MPa and 1.47 MPa, and that of desert facies sandstone was 23.47 MPa and 1.11 MPa. Obviously, the UCS and the TS of braided river facies sandstone were higher than those of desert facies sandstone in the natural state. When the sandstone was fully saturated, the UCS of braided river facies sandstone and desert facies sandstone decreased to 11.01 MPa and 8.45 MPa, and the decay rates were 41.24% and 35.93%, respectively. In addition, the TS decreased to 0.48 MPa and 0.30 MPa, and the decay rates were 32.90% and 26.98%, respectively.

3.2. Effect of Water on AE Energy

The AE energy is directly related to the intensity of the AE impact signal, which can truly reflect the scale of rock internal fractures. Figures 4 and 5 represent the changes in the load and AE energy over time in the TS and UCS tests, respectively. The figures show that AE energy is released to varying degrees during tests on sandstones in different states. As shown in Figure 4a,c, the cumulative AE energy–time curve of the natural state sandstone had two diversions. In the early stage of loading, local stress concentration occurs inside the sample, the cementation between mineral particles was damaged, microcracks appeared and a large amount of AE energy (>150 mV·ms) was released, resulting in the first cumulative AE energy step. In the elastic deformation stage, the AE activities entered the quiet period, and the amount of AE energy released was smaller (<100 mV·ms). As the load increased, the cracks in the sample gradually linked, and finally completely connected, and the sample was damaged. A lot of energy was released in this stage, resulting in the second cumulative AE energy step, the AE energy reached the maximum, and the sample underwent brittle failure. However, the cumulative AE energy–time curve of saturated sandstone had largely differed from the natural state, as shown in Figure 4b,d. This difference was due to the weakening effect of water, which loosened the internal cementation of saturated sandstone, and the bearing capacity was mainly provided by mineral particles. As the load increased, the AE energy of saturated sandstone was released continuously, and the cumulative AE energy increased steadily without an obvious sudden step. Under the peak load, the sandstone was damaged, and the AE energy reached the maximum value. During the whole loading process, the cumulative AE energy released by braided river facies sandstone and desert facies sandstone in the natural state was 12.89 $\times$ 10^3 mV·ms and 7.49 $\times$ 10^3 mV·ms, respectively, which was much larger than the energy releases of 5.55 $\times$ 10^3 mV·ms and 4.36 $\times$ 10^3 mV·ms in the saturated state, respectively.

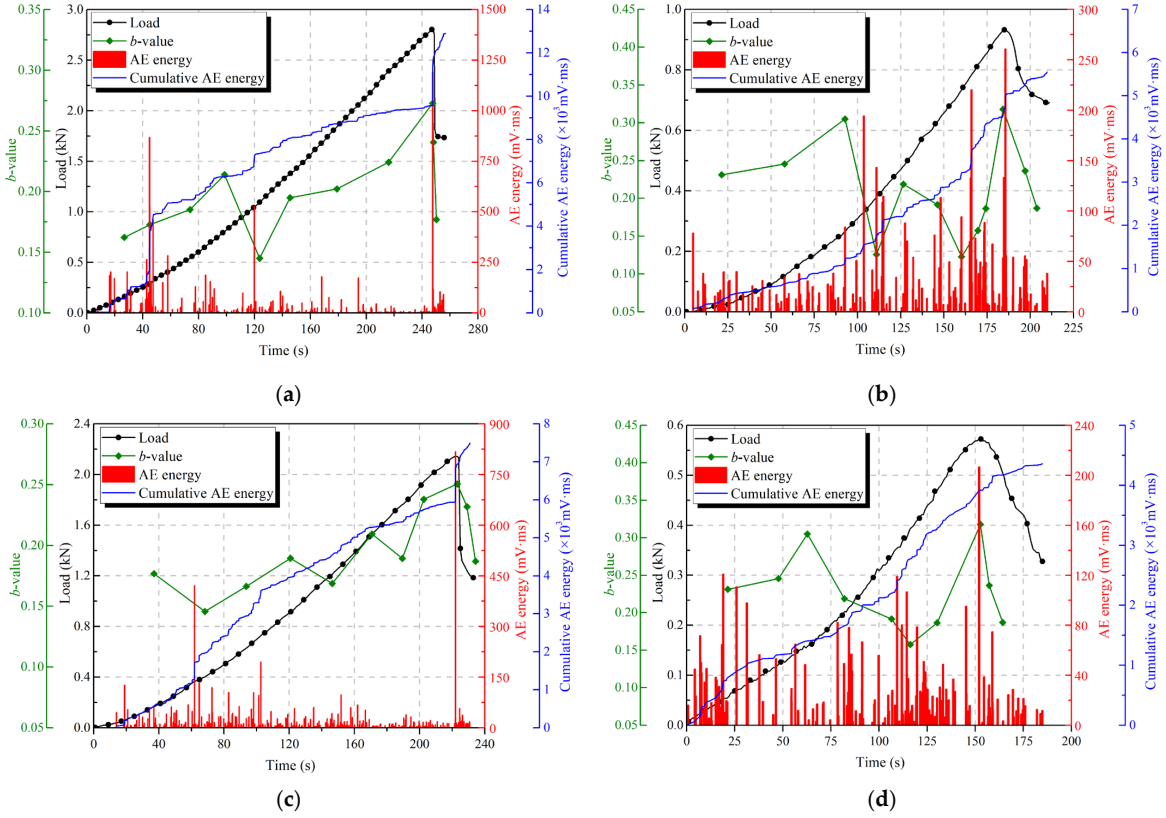


Figure 4. The evolution of the load and AE energy during the Brazilian disc test: (**a**) B-BN-1; (**b**) B-BS-2; (**c**) B-DN-1; (**d**) B-DS-1.

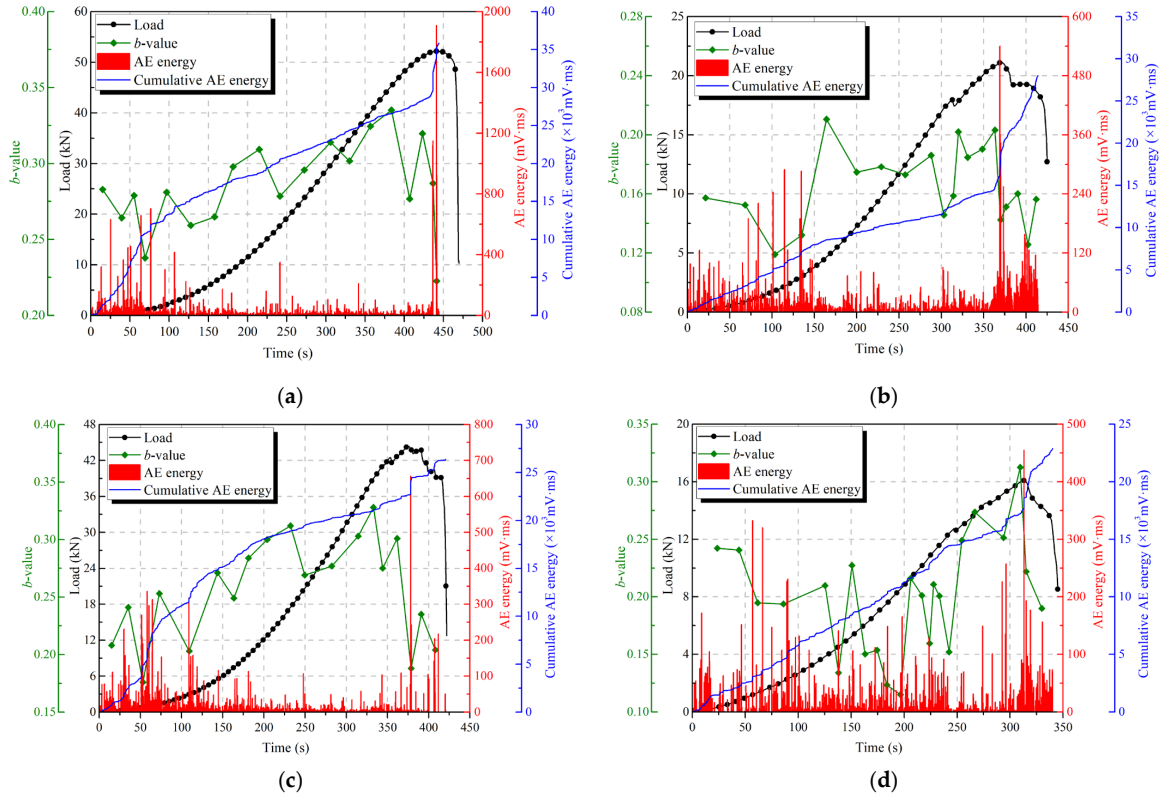


Figure 5. The evolution of the load and AE energy during the uniaxial compressive test: (**a**) C-BN-2; (**b**) C-BS-1; (**c**) C-DN-1; (**d**) C-DS-3.

Figure 5 shows that the AE energy variation in sandstone in the uniaxial compressive test was similar to that in the Brazilian test. Figure 5 shows that the AE energy of each sample was larger in the initial stage of compaction, and the AE energy of natural sandstone was greater than that of saturated sandstone. In this stage, the natural state sandstone appeared to be the first accumulated AE energy "step". Then, it entered the quiet period in the elastic stage, in which continuous micro AE events occurred, and the AE energy was weak in this period. As the axial force increased, microcracks gradually developed in the sample. When the final failure occurred, the AE energy reached the maximum, and the second obvious step occurred in the cumulative AE energy. However, for the saturated sandstone, the cumulative AE energy–time curve had only one step at the peak failure point. Before this point, as the load increased, small fractures appeared in the sample as the AE energy was continuously released. The cumulative AE energy curve increased steadily over time. The AE energy of saturated sandstone was always less than that of natural sandstone, and the cumulative AE energy of saturated braided fluvial facies sandstone and desert facies sandstone was 26.38 $\times$ 10^3 mV·ms and 22.88 $\times$ 10^3 mV·ms, respectively, which was much less than those of natural sandstone (35.83 $\times$ 10^3 mV·ms for braided fluvial facies and 27.99 $\times$ 10^3 mV·ms for desert facies).

3.3. The b-Value of the AE

The AE amplitude represents the maximum amplitude of a single AE event, and it is used to characterize the strength of the AE event. Its size depends on the size of cracks in rock samples, and its unit is dB. The *b*-value describes the relationship between the magnitude and frequency of earthquakes. In 1955, Gutenberg and Richter [27] found that the frequency of earthquakes decreases exponentially with magnitude, and they used the parameter *b* to describe the proportion of the source scale distribution. Scholars have found that the magnitude of AE events during the rock loading process follows a power-law distribution, similar to the cumulative frequency–amplitude relationship observed during earthquakes [28]. For AE events that occurred during loading of rocks, which manifests as seismic activity, the improved Gutenberg–Richter relationship (Equation (2)) can be used to calculate the variation in the *b*-value during rock deformation and failure [13,27,29]:

$$LogN(\geq A) = a - bM, \tag{2}$$

where A is the AE amplitude during loading; N is the number of AE hits in a particular time window with an amplitude greater than A; a and b are constants; and M is the magnitude of the earthquake, which is usually represented by the AE amplitude divided by 20, i.e., $M = A/20$. The *b*-value represents the ratio of the microcrack to the macrocrack frequency. An increase in the *b*-value means that the proportion of small events increases, and the sample is dominated by small-scale fractures; in contrast, a decrease in the *b*-value indicates that the proportion of large events increases, and the number of large-scale microfractures increases [30,31]. Previous research proposed that the number of events on which the b-value calculation would be based does not affect the results [13,32], so a sliding time window was used to analyze the variation of the b-value during tests.

The variation in the *b*-value over time during loading was calculated by counting the amplitudes of AE events in the Brazilian disc test and uniaxial compression test. In the Brazilian disc test (Figure 4), the *b*-value of natural sandstone increased before the peak stress, fluctuated obviously when the high-energy signal was released and decreased after the peak stress. Moreover, the *b*-value of saturated sandstone fluctuated sharply before the peak stress, and the change after the peak stress was the same as that of natural sandstone. The main reasons for this change are as follows: before the peak point, as load increased, the microcracks in the sample gradually began to generate and expand, the small-sized cracks increased rapidly and the large-sized cracks increased relatively slowly, leading to an increase in the *b*-value. Once a large-scale fracture occurred, the AE energy was released, and the *b*-value decreased accordingly. When the load gradually approached the peak point, the microcracks were connected to each other, and the large

cracks increased rapidly, resulting in a rapid decrease in the *b*-value. Due to the weakening of cementation between mineral particles in sandstone by water, microfractures were produced; thus, large-scale cracks formed easily in saturated sandstone during loading, causing the *b*-value to fluctuate greatly. Figure 5 shows a similar variation in the *b*-value in the uniaxial compression test, and the only difference was that the point at which the *b*-value in natural sandstone suddenly decreases appears before the peak value. This shows that under uniaxial compression, the process from macrocrack formation to natural rock instability was relatively long. Under the action of load splitting and saturation, sandstone was mainly subjected to sudden macroscopic failure.

3.4. Effect of Water on the AE Peak Frequency

The peak frequency of each AE event can be obtained by analyzing the spectrum of the AE signal collected during the test [17]. Due to the influence of their own fabric, shape and loading mode, rock samples showed different peak frequency distributions of AE signals in different states. The structural characteristics of rock samples after soaking were different; therefore, AE signals with different peak frequency characteristics were generated in the process of deformation and failure.

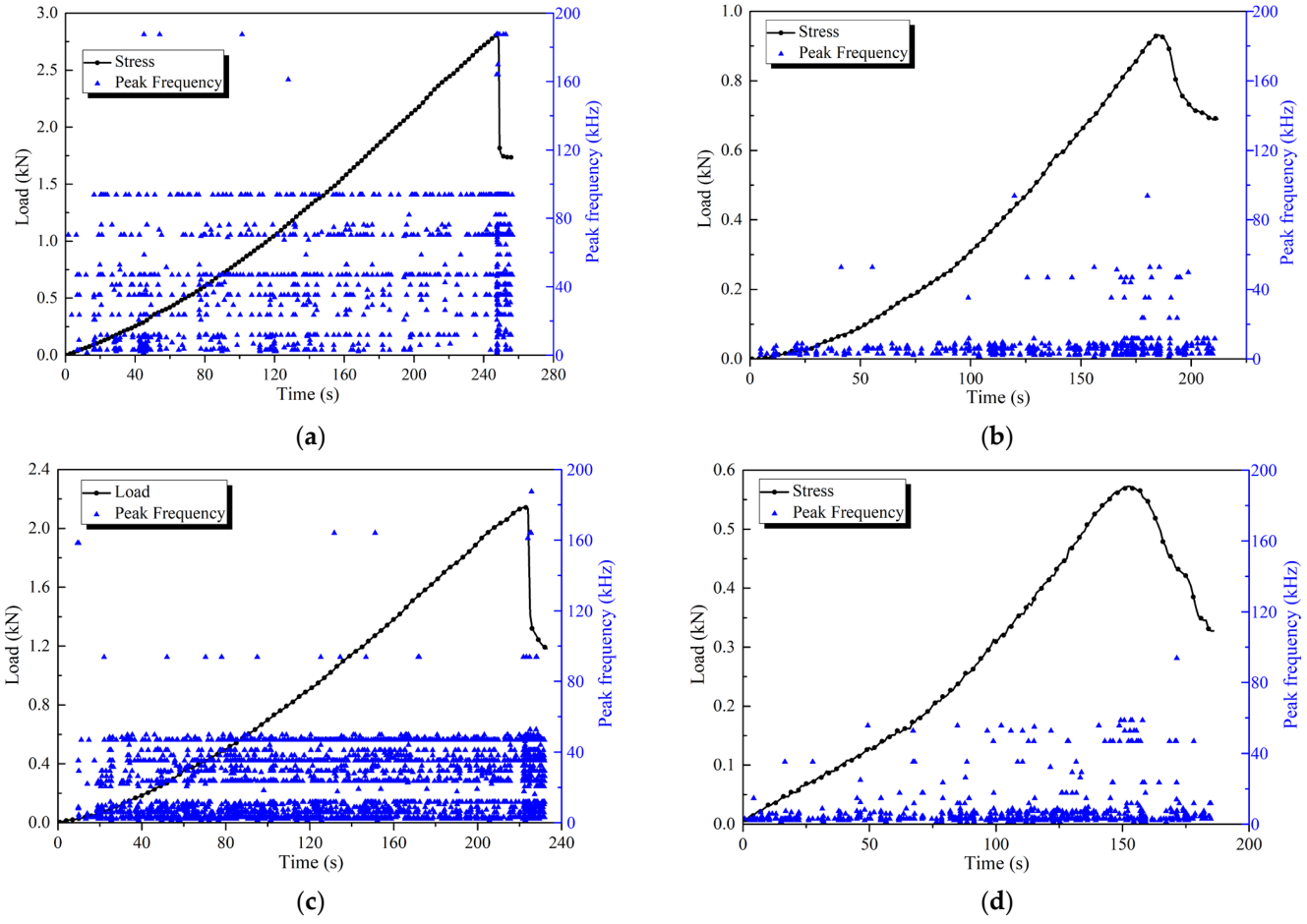


Figure 6. Relationship between the load, time and AE signal peak frequency during the Brazilian test: (**a**) B-BN-1; (**b**) B-BS-2; (**c**) B-DN-1; (**d**) B-DS-1.

Figure 6 shows the AE peak frequency distribution and load variation over time in the Brazilian disc test. The peak frequency distribution was chaotic and scattered in the initial compaction stage. During the whole process of loading, the peak frequency distribution range of natural sandstone was wider than that of saturated sandstone, and there were more AE signals. The AE frequency of indoor rocks is within the range of 10–500 kHz,

and below 10 kHz is regarded as noise [33]. For natural sandstone, the peak frequency was mainly distributed in the ranges of 10~50 kHz and 90~100 kHz, and there was a small distribution in the high-frequency band above 160 kHz. In addition, a small distribution occurred in the range of 60~80 kHz for the braided river facies sandstone. When brittle failure occurred, the AE signals in the range of 10~80 kHz increased obviously, and they also appeared in the range of 160~200 kHz. For the saturated sandstone, the peak frequency was mainly distributed in the frequency band of 10~20 kHz. When the samples entered the linear evolution stage, the signals began to appear in the frequency band of 30~60 kHz, and the AE signals increased and concentrated when the sample was damaged.

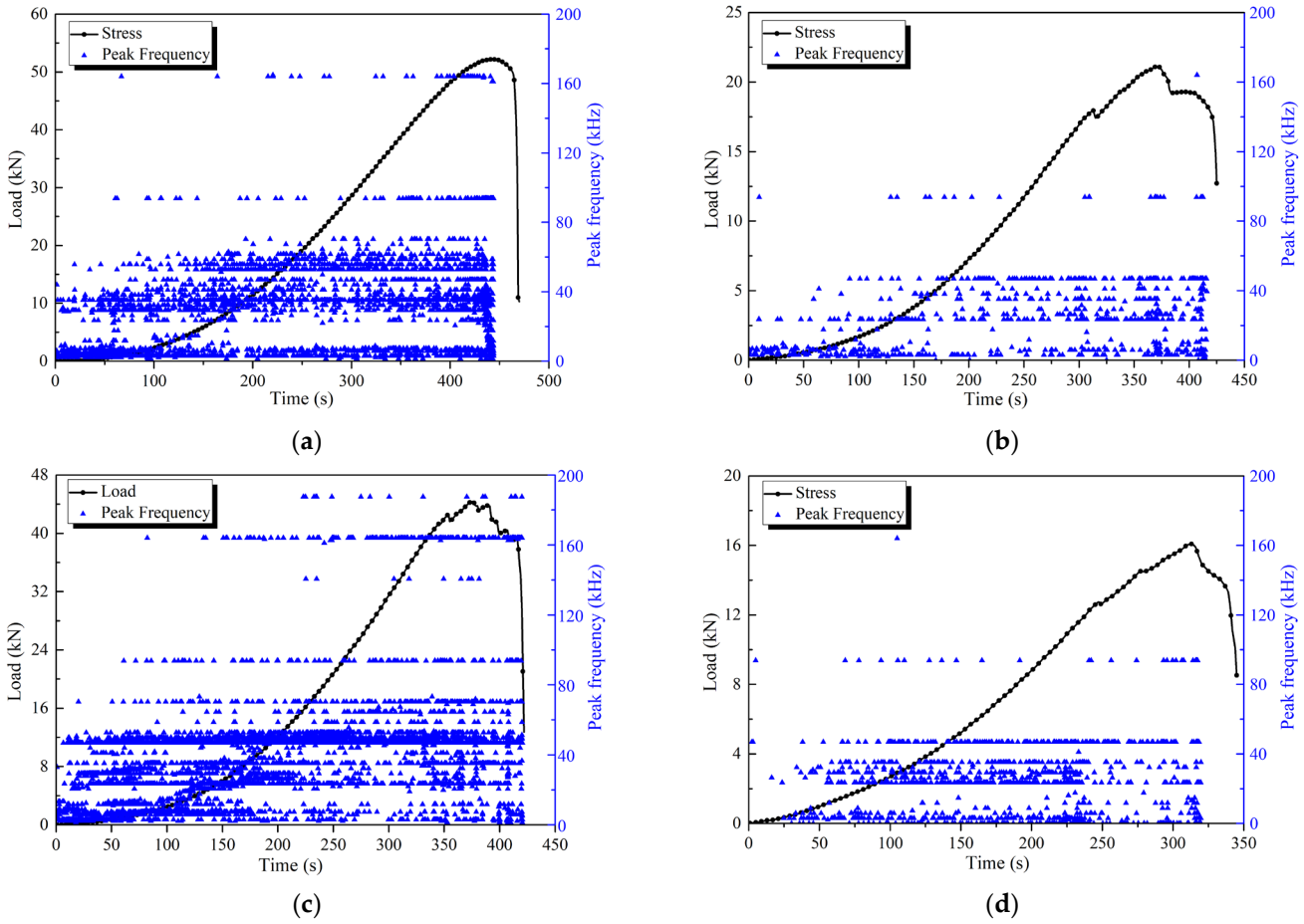


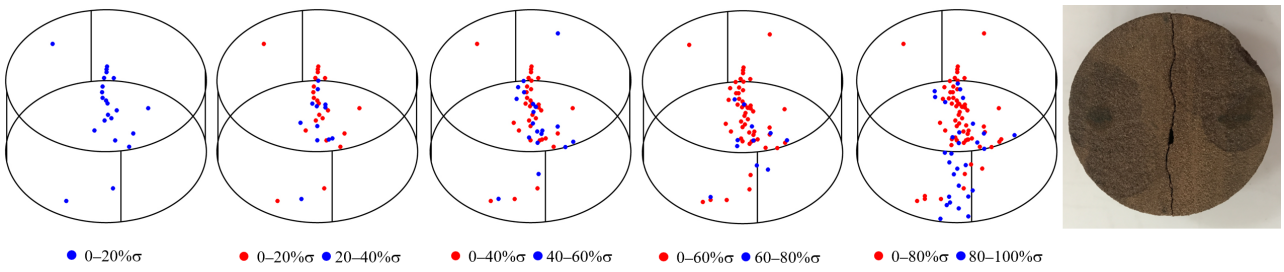
Figure 7. Relationship between the load, time and AE signal peak frequency during the UCS test: (**a**) C-BN-2; (**b**) C-BS-1; (**c**) C-DN-1; (**d**) C-DS-3.

Figure 7 shows that the change in the AE peak frequency in the uniaxial compression test was more obvious. For the braided river facies sandstone in the natural state as shown in Figure 7a, the peak frequency was mainly distributed in the range of 30~40 kHz initially and then appeared occasionally in another frequency band of 20~80 kHz. As the loading increased, the distribution range of the peak frequency became larger. The signals at 40~70 kHz, 90 kHz and 160 kHz gradually appeared and became denser. Before the failure of the samples, the AE peak frequencies were no longer dispersed but were densely distributed in each frequency band. At this time, the sandstone was at the critical fracture point. The variation in the AE peak frequency of the desert facies sandstone in the natural state was basically the same as that of the braided river facies, but there were two differences: (1) an obvious dense distribution at 50 kHz occurred initially; and (2) more signals were generated in the high-frequency band (mainly at 140 kHz and 190 kHz) as the loading increased. The AE peak frequency distribution in the saturated state was obviously different from that in the natural state. The AE

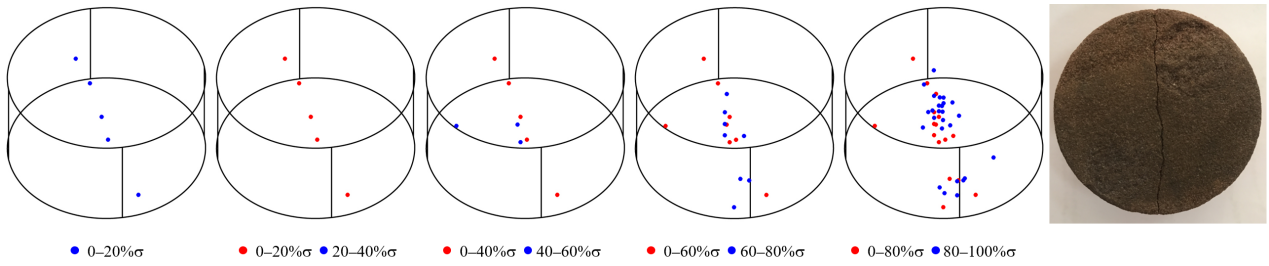
signals of the saturated sandstone were mainly distributed in two ranges: 10~50 kHz and 90 kHz. Compared with the natural state, the signals were obviously missing in the range of 50~70 kHz. In addition, there were concentrated AE signals near the destruction point, but they were not as obvious as those in the natural state.

3.5. Spatial Evolution of AE Events

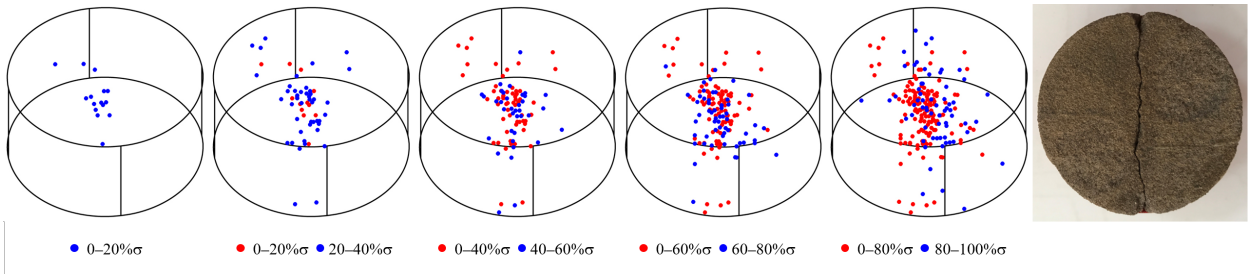
The spatial location of each AE event requires at least four AE sensors to detect AE events, and the location of each event has independent spatial coordinates and AE parameters [15]. To some extent, the generation and spatial evolution of AE events can reflect the generation, aggregation and expansion of microcracks in the sample. The dense distribution of AE events indicates that the cracks propagate strongly.



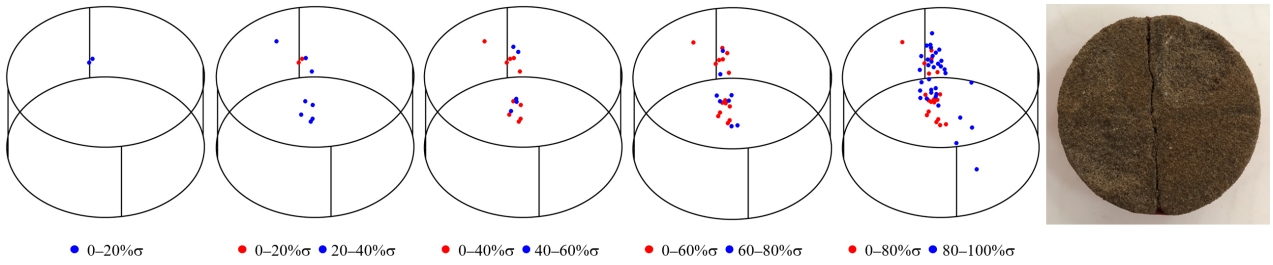
(**a**)



(**b**)

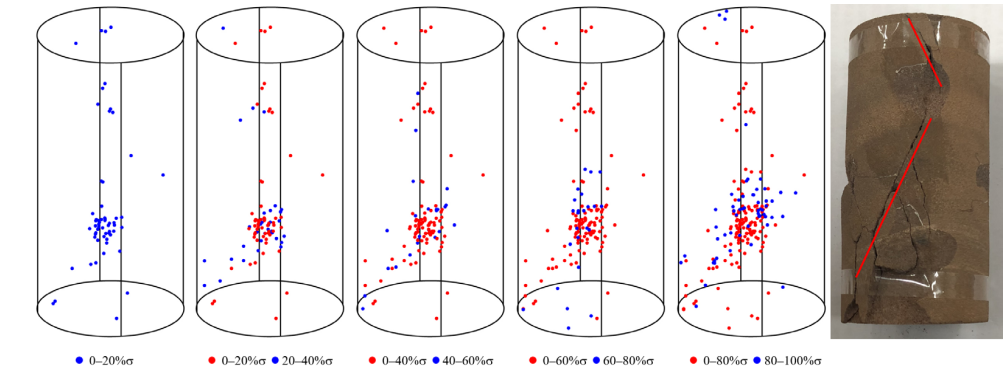


(**c**)

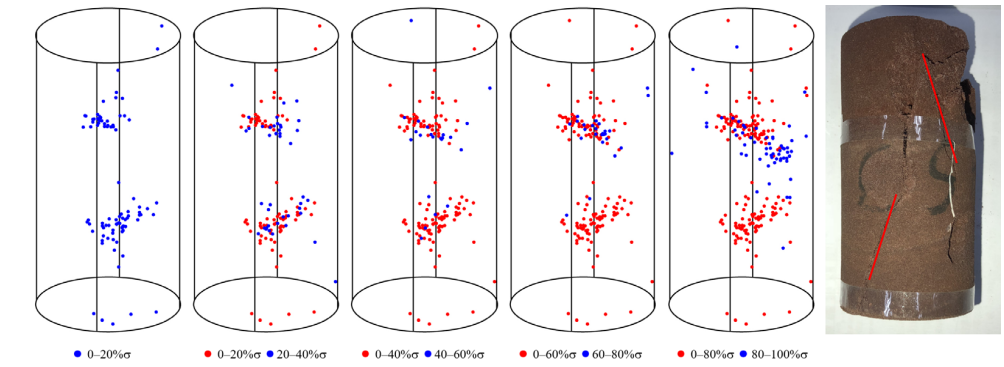


(**d**)

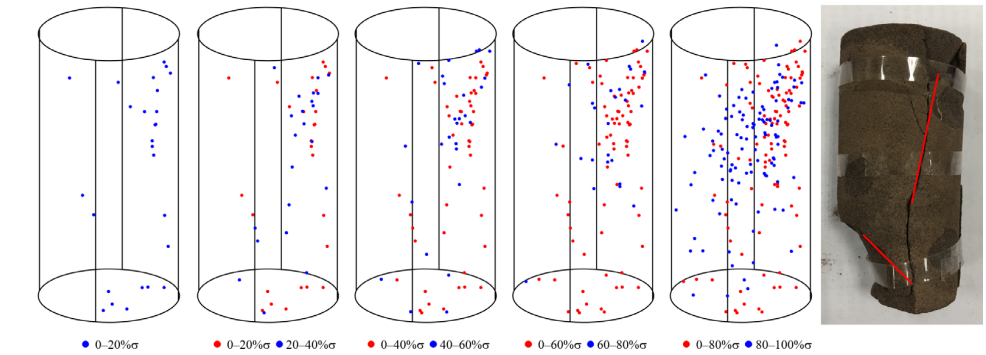
Figure 8. Spatial evolution of AE events in the Brazilian test: (**a**) B-BN-1; (**b**) B-BS-2; (**c**) B-DN-1; (**d**) B-DS-1.



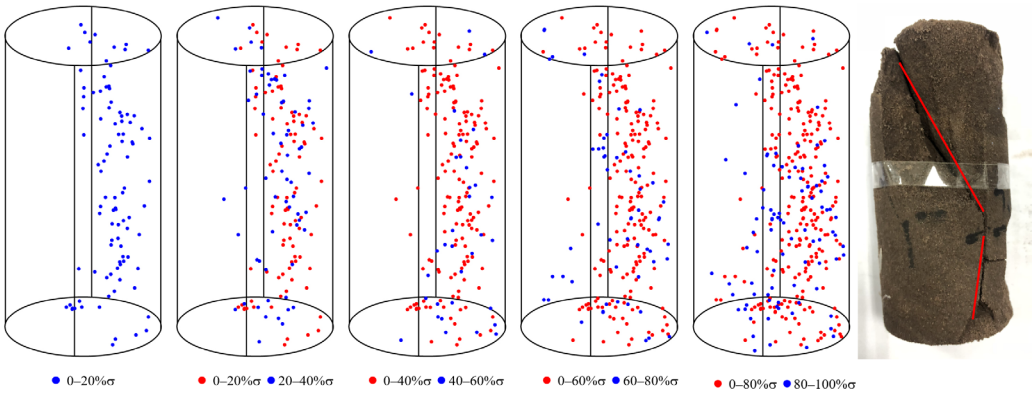
(**a**)



(**b**)



(**c**)



(**d**)

Figure 9. Spatial evolution of AE events in the uniaxial compressive test: (**a**) C-BN-2; (**b**) C-BS-1; (**c**) C-DN-1; (**d**) C-DS-3.

Figure 8 shows the spatial evolution of AE events in different pre-peak stages under splitting conditions. The blue dots represent the new AE events in this stage, and the red dots represent all the AE events before this stage. Figure 8a,c show that in the initial stage of loading, AE events occurred on both sides of the fracture surface of sandstone in the natural state, and they rapidly appeared as the load increased. Finally, microcracks connected with each other and resulted in a macro fracture surface, which indicates that the sandstone failed. For the saturated sandstone, as shown in Figure 8b,d, there were fewer AE events in the initial stage of loading. As the loading increased, AE events occurred slowly. After entering the crack propagation stage, relatively concentrated AE events occurred rapidly, and macro fractures appeared in the middle of the sample, resulting in the failure of the sandstone. The AE events in the braided river facies sandstone mainly occurred along the middle fracture surface, while the AE events of desert facies sandstone mainly extended from the center of the sample to both sides.

Figure 9 shows the spatial evolution of AE events in sandstone subjected to uniaxial compression. In the initial stage of loading, many AE events occurred in the sandstone samples. As the loading increased, the growth rate of AE events decreased, but AE events always developed along both sides of the main fracture surface. A large number of AE events were generated quickly before the peak strength was reached, and microcracks connected with each other to form a macro fracture surface, which finally resulted in the rock failure. Figure 9a,b show that during the loading process, the AE events in the braided river facies sandstone were relatively concentrated, mainly along two intersecting fracture surfaces, while the AE events occurred along both sides of the main fracture surface in the desert facies sandstone (Figure 9c,d). Generally, the number of AE events in the desert facies sandstone was more than that in the braided river facies sandstone, and the distribution was more dispersed, which resulted in the desert facies sandstone breaking into multiple blocks of different sizes after failure, and the degree of sample fragmentation was higher than that of braided river facies sandstone. The AE spatial location in the natural sandstone was less than that in the saturated sandstone in the uniaxial compression test. The reason for this difference was that brittle failure occurred in the natural sandstone, while brittle-plastic failure appeared in the saturated sandstone due to water weakening. In addition, there were more microfractures in the saturated sandstone.

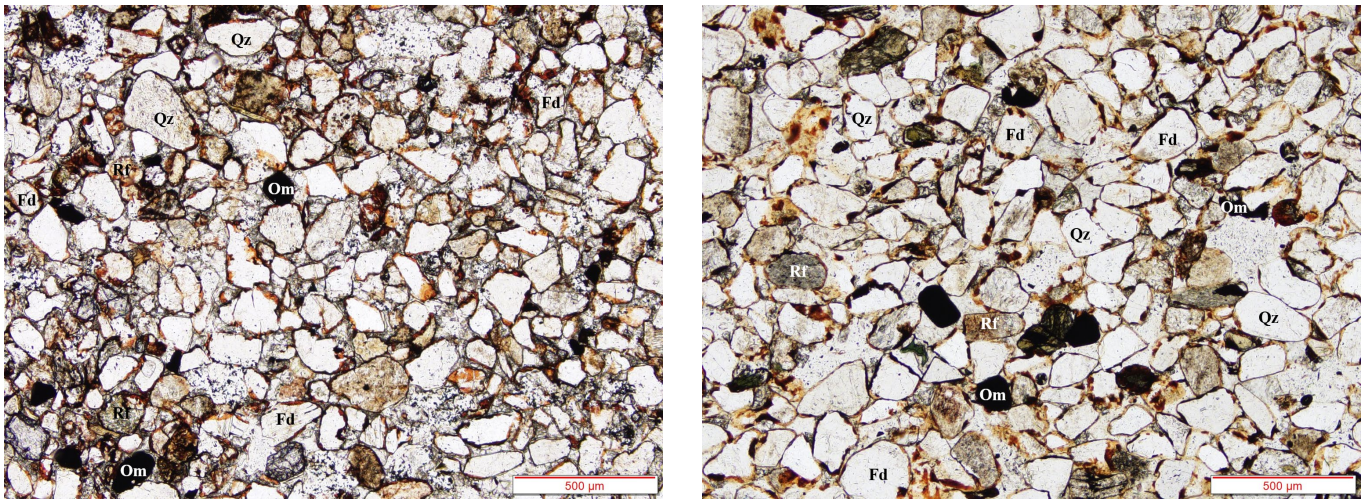
4. Discussion

The sandstones from two different sedimentary facies mainly have subrounded to subangular grains, and medium sorting, as shown in Figure 10. The contacts between mineral grains are mainly point-line contacts. The braided river facies sandstone is mainly pack-pore cementation, and the pores between grains are filled with argillaceous cement. The desert facies sandstone exhibits contact cementation with less cement in the pores, and the argillaceous components are mainly concentrated at the grain contacts. The desert facies sandstone has more pores, so it has a higher water content in the saturated state.

When rock is soaked in water, a series of physical-chemical effects occur, including mineral dissolution and water–rock interactions [34]. Once the rock is soaked in water, argillaceous cements and clay minerals are dissolved first, and then microcracks appear in the cement, causing a loose internal microstructure, as shown in Figure 11b. This may reduce the friction coefficient of rock to 40~80% of the original friction coefficient [35]. Then, orthoclase and albite in sandstone undergo water–rock chemical reactions, and secondary minerals such as kaolinite are produced and adhere to cracks and pores. The typical reaction equations are as follows [36]:

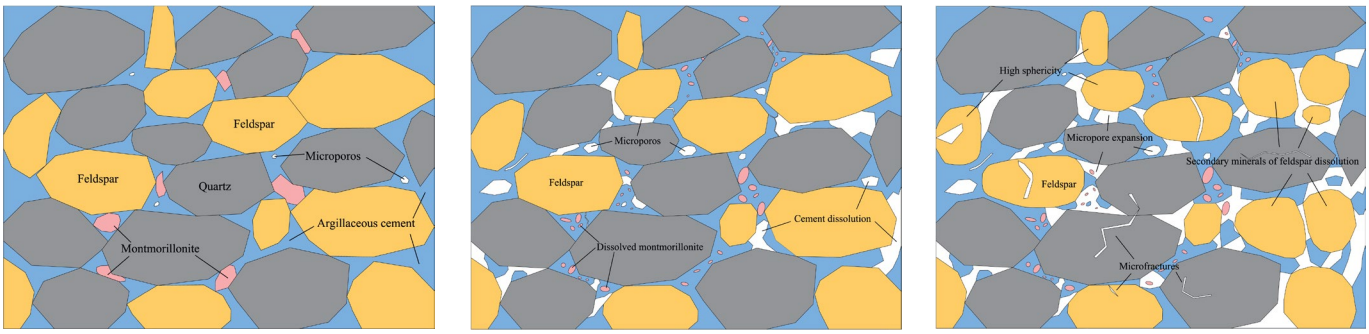
$$2Na(Al_2Si_3O_8)+3H_2O = 2Na^+ +2OH^- +4SiO_2+Al_2(Si_2O_5)(OH)_4 \downarrow, \quad (3)$$

$$2K(AlSi_3O_8)+3H_2O = 2K^+ +2OH^- +4SiO_2+Al_2(Si_2O_5)(OH)_4 \downarrow \quad (4)$$



(**a**) (**b**)

Figure 10. Micrograph of a microstructural slice of fine sandstone: (**a**) braided fluvial facies; (**b**) desert facies (Qz, quartz; Fd, feldspar; Rf, rock fragments; Om, organic matter).



(**a**) (**b**) (**c**)

Figure 11. Schematic diagram of the water–rock interaction process: (**a**) combination of mineral particles and argillaceous cement; (**b**) dissolution of clay minerals and cements; (**c**) mineral dissolution and crack generation (modified from Hu et al. 2018 [36]).

In the feldspar dissolution process, insoluble minerals precipitate in internal microcracks and pores in rocks, resulting in crystallization pressure, which further promotes the development of micropores and fractures in samples (Figure 11c). This series of chemical and physical actions in rock sample interiors causes the rock microstructure to change considerably and further leads to the weakening of rock strength. In addition, capillary force and effective pressure are reduced by the water in the pores and fractures, resulting in the mechanical properties being weakened [37].

The X-ray diffraction (XRD) spectra of Cretaceous sandstone from two different sedimentary facies are shown in Figure 12. Their mineral compositions and contents are different. The mineral compositions of the two sandstones with different sedimentary facies are shown in Table 2. The quartz content of braided fluvial facies sandstone (33.32%) is significantly higher than that of desert facies sandstone (22.96%). Scholars have proven that this grain is stiffer and has a greater integrity [38,39]. Thus, the UCS and TS of braided fluvial facies sandstone are obviously greater than those of desert facies sandstone. Moreover, the maximum AE energy released during failure is greater, and the cumulative AE energy during the whole loading process is also greater.

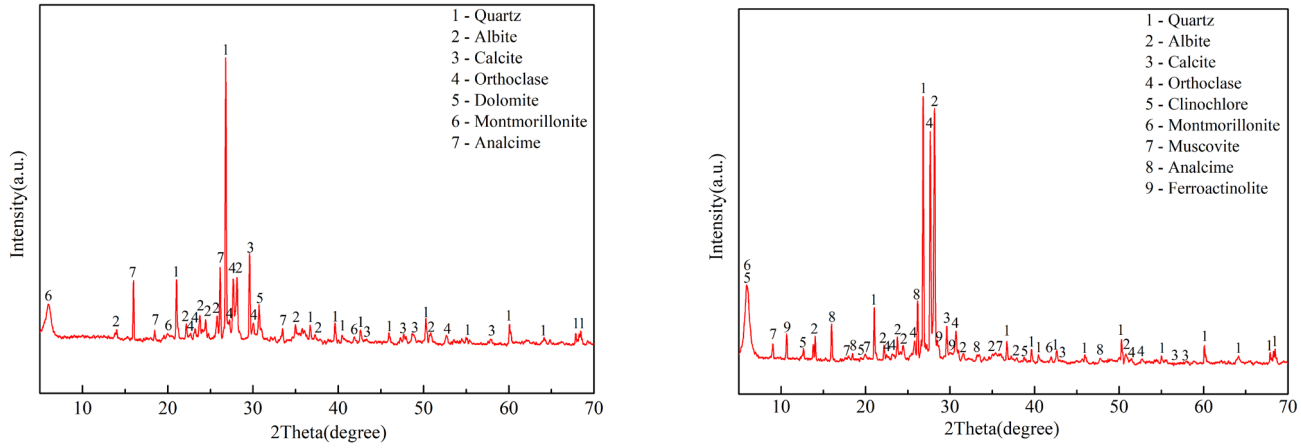


Figure 12. XRD spectrum of Cretaceous sandstone: (**a**) braided fluvial facies; (**b**) desert facies.

Table 2. Mineral composition analysis of Cretaceous sandstone (weight %).

Sedimentary Facies	Quartz	Albite	Orthoclase	Calcite	Muscovite	Montmorillonite	Analcime	Others
Braided fluvial facies	33.32	18.14	23.01	5.26	-	3.2	12.51	4.56
Desert facies	22.96	29.32	23.15	2.73	9.23	0.92	6.43	5.26

It should be noted that the feldspar content in the two sedimentary facies sandstones is relatively high (41.15% in the braided river facies sandstone and 52.47% in the desert facies sandstone). The hydro-chemical reaction between feldspar and water decreases the UCS and TS of saturated sandstone to varying degrees.

Due to the high feldspar content in the desert facies sandstone, the decomposition of feldspar due to saturation has a greater influence on its mechanical properties than that of the braided fluvial sandstone. After soaking, the UCS and TS of the braided river facies sandstone were reduced by 58.76% and 67.10%, respectively, while the desert facies sandstone was reduced by 64.03% and 73.02%. The degree to which the mechanical properties of desert facies sandstone are weakened was greater than that of braided river facies sandstone.

5. Conclusions

In this study, the natural and saturated weakly cemented Cretaceous sandstones with different sedimentary facies were used to carry out Brazilian splitting tests and uniaxial compression tests, and AE characteristics were monitored simultaneously. The main conclusions are as follows.

(1) Water weakened the mechanical properties of weakly cemented Cretaceous sandstone. The UCS of the saturated braided fluvial facies and desert facies sandstone decreased to 41.24% and 32.90% of the natural state, respectively. The TS decreased to 35.90% and 26.98% compared to the natural sandstone, respectively.

(2) The AE energy and *b*-value corresponded well with the load–time curve, and the failure of the sample was accompanied by the release of a large amount of AE energy and the rapid decrease in the *b*-value. In saturated sandstone, water destroys the cementation between mineral particles, initiates microcracks in the sample and reduces the cumulative AE energy; in addition, the *b*-value fluctuates greatly during loading. The distribution range of the AE peak frequency in natural sandstone was wider than that in saturated sandstone.

(3) The spatial location of AE events reflects the development of microcracks during loading. There were almost no microcracks in the saturated sandstone during the early stage of the Brazilian splitting test, and a large number of AE events occurred rapidly near the peak, leading to the failure of samples. However, in the process of uniaxial compression,

due to the weakening of water, there were more microcracks in the saturated sandstone than in the natural state sandstone.

(4) The high quartz content was the reason why the strength of the braided fluvial facies sandstone was higher than that of the desert facies sandstone. The dissolution of argillaceous cement and feldspar resulted in a decrease in the strength of the saturated sandstone. The high feldspar content led to the higher weakening degree of the desert facies sandstone.

Author Contributions: Methodology, data curation, writing—original draft preparation, Y.Y.; conceptualization, funding acquisition, writing—review and editing, W.L.; writing—review and editing, Q.L. All authors have read and agreed to the published version of the manuscript.

Funding: This research was funded by the State Key Program of National Natural Science Foundation of China (Grant No. 41931284), the project of "Enlisting and Leading" of China Coal (No. 2022JB01), the Natural Science Foundation of Jiangsu Province (BK20190646), the Graduate Innovation Program of China University of Mining and Technology (2022WLKXJ038) and the Postgraduate Research & Practice Innovation Program of Jiangsu Province (KYCX22_2605).

Institutional Review Board Statement: Not applicable.

Informed Consent Statement: Not applicable.

Data Availability Statement: The data used to support the findings of this study are available from the corresponding author upon request.

Conflicts of Interest: The authors declare no conflict of interest.

References

1. Chigira, M.; Imai, C.; Hijikata, H. Water percolating behavior indicated by the water chemistry within a decomposed granite slope, central Japan. *Eng. Geol.* **2006**, *84*, 84–97. [CrossRef]
2. Hong, J.M.; Chen, Y.F.; Liu, M.M.; Zhou, C.B. Inverse modelling of groundwater flow around a large-scale underground cavern system considering the excavation-induced hydraulic conductivity variation. *Comput. Geotech.* **2017**, *81*, 346–359. [CrossRef]
3. Erguler, Z.A.; Ulusay, R.B. Water-induced variations in mechanical properties of clay-bearing rocks. *Int. J. Rock Mech. Min. Sci.* **2009**, *46*, 355–370. [CrossRef]
4. Wu, F.; Qi, S.; Lan, H. Mechanism of uplift deformation of the dam foundation of Jiangya water power station, Hunan Province, P.R. China. *Hydrogeol. J.* **2005**, *13*, 451–466.
5. Wen, B.P.; He, L. Influence of lixiviation by irrigation water on residual shear strength of weathered red mudstone in Northwest China: Implication for its role in landslides' reactivation. *Eng. Geol.* **2012**, *151*, 56–63. [CrossRef]
6. Işık, Y. Influence of water content on the strength and deformability of gypsum. *Int. J. Rock Mech. Min. Sci.* **2010**, *47*, 342–347.
7. Zhou, Z.L.; Cai, X.; Cao, W.Z.; Li, X.B.; Xiong, C. Influence of water content on mechanical properties of rock in both saturation and drying processes. *Rock Mech. Rock Eng.* **2016**, *49*, 3009–3025. [CrossRef]
8. Rajabzadeh, M.A.; Moosavinasab, Z.; Rakhshandehroo, G. Effects of rock classes and porosity on the relation between uniaxial compressive strength and some rock properties for carbonate rocks. *Rock Mech. Rock Eng.* **2012**, *45*, 113–122. [CrossRef]
9. Masoumi, H.; Horne, J.; Timms, W. Establishing empirical relationships for the effects of water content on the mechanical behavior of Gosford sandstone. *Rock Mech. Rock Eng.* **2017**, *50*, 2235–2242. [CrossRef]
10. Chang, C.; Haimson, B. Effect of fluid pressure on rock compressive failure in a nearly impermeable crystalline rock: Implication on mechanism of borehole breakouts. *Eng. Geol.* **2007**, *89*, 230–242. [CrossRef]
11. Meng, L.; Wang, H.W.; Li, X.H.; Zhao, X.Y. Investigation on acoustic emission characteristics in failure process of coal absorbed methane. *J. China Coal Soc.* **2014**, *39*, 377–383.
12. Pradhan, S.; Stroisz, A.M.; Fjar, E.; Stenebraten, J.F.; Lund, H.K.; Sonstebo, E.F. Stress-induced fracturing of reservoir rocks: Acoustic monitoring and uct image analysis. *Rock Mech. Rock Eng.* **2015**, *48*, 2529–2540. [CrossRef]
13. Ge, Z.L.; Sun, Q. Acoustic emission (ae) characteristics of granite after heating and cooling cycles. *Eng. Fract. Mech.* **2018**, *200*, 418–429. [CrossRef]
14. Han, Q.; Yang, G.; Xu, J.; Fu, Z.; Giuseppe, L.; Alberto, C. Acoustic emission data analyses based on crumb rubber concrete beam bending tests. *Eng. Fract. Mech.* **2018**, *210*, 189–202. [CrossRef]
15. Shi, G.C.; Yang, X.J.; Yu, H.C.; Zhu, C. Acoustic emission characteristics of creep fracture evolution in double-fracture fine sandstone under uniaxial compression. *Eng. Fract. Mech.* **2019**, *210* (Suppl. S1), 13–28. [CrossRef]
16. Geng, J.S.; Cao, L.W. Failure analysis of water-bearing sandstone using acoustic emission and energy dissipation. *Eng. Fract. Mech.* **2020**, *231*, 107021. [CrossRef]
17. Ji, H.G.; Lu, X. Characteristics of acoustic emission and rock fracture precursors of granite under conventional triaxial. *Chin. J. Rock Mech. Eng.* **2015**, *34*, 694–702.

18. Noorsuhada, M.N. An overview on fatigue damage assessment of reinforced concrete structures with the aid of acoustic emission technique. *Constr. Build. Mater.* **2016**, *112*, 424–439. [CrossRef]
19. You, S.; Ji, H.G.; Wang, T.; Song, Z.Y. Thermal and mechanical coupling effects on permeability of weakly cemented sandstone. *Emerg. Mater. Res.* **2018**, *7*, 100–108. [CrossRef]
20. Wang, L.; Qin, Y.; Jia, H.B.; Su, H.M.; Chen, S.G. Study on mechanical properties and energy dissipation of frozen sandstone under shock loading. *Shock. Vib.* **2020**, *2020*, 8893128. [CrossRef]
21. Xu, H.; Shao, Z.; Wang, Z.; Cai, L.; Jiang, X. Sub-level classification and prediction system of fully weathered red sandstone rock mass based on physical property indices. *KSCE J. Civ. Eng.* **2021**, *25*, 1066–1085. [CrossRef]
22. Cai, J.L.; Zou, W. Triaxial compressive failure characteristics and constitutive model study of Jurassic-Cretaceous weakly cemented sandstone. *Adv. Civ. Eng.* **2020**, *2020*, 8812575. [CrossRef]
23. Chen, W.C.; Li, W.P.; He, J.H.; Qiao, W.; Wang, Q.Q.; Yang, Y.R. Impact of mining-induced bed separation spaces on a cretaceous aquifer: A case study of the Yingpanhao coalmine, Ordos Basin, China. *Hydrogeol. J.* **2022**, *30*, 691–706. [CrossRef]
24. He, J.H.; Li, W.P.; Qiao, W.; Yang, Z.; Li, L.N. Establishment and application of bed-separation water inrush coefficient method considering water resistance of fractured rock mass. *Geofluids* **2022**, *2022*, 8978653. [CrossRef]
25. Ulusay, R.; Hudson, J.A. The complete ISRM suggested methods for rock characterization, testing and monitoring: 1974-2006. In *Suggested Methods Prepared by the ISRM Commission on Testing Methods*; International Society for Rock Mechanics: Lisbon, Portugal, 2007.
26. Li, H. Research progress on evaluation methods and factors influencing shale brittleness: A review. *Energy Rep.* **2022**, *8*, 4344–4358. [CrossRef]
27. Gutenberg, B.; Richter, C.F. Seismicity of the earth and associated phenomenon. *J. Geol.* **1955**, *63*, 588.
28. Lockner, D.A. The role of AE in the study of rock fracture. *Int. J. Rock Mech. Min.* **1993**, *30*, 883–899. [CrossRef]
29. Datt, P.; Kapil, J.C.; Kumar, A. Acoustic emission characteristics and b-value estimate in relation to waveform analysis for damage response of snow. *Cold Reg. Sci. Technol.* **2015**, *119*, 170–182. [CrossRef]
30. Scholz, C.H. On the stress dependence of the earthquake b value. *Geophys. Res. Lett.* **2015**, *42*, 1399–1402. [CrossRef]
31. Lockner, D.A.; Byerlee, J.D.; Kuksenko, V. Quasi-static fault growth and shear fracture energy in granite. *Nature* **1991**, *350*, 39–42. [CrossRef]
32. Carpinteri, A.; Lacidogna, G.; Manuello, A. The b-value analysis for the stability investigation of the ancient athena temple in syracuse. *Strain* **2011**, *47* (Suppl. S1), e243–e253. [CrossRef]
33. Zhu, J.; Deng, J.H.; Chen, F.; Huang, Y.M. Moisture-induced softening characteristics and mechanisms of saturated hard rocks under compression. *Chin. J. Geotech. Eng.* **2023**, *45*, 768–776.
34. Galouei, M.; Fakhimi, A. Size effect, material ductility and shape of fracture process zone in quasi-brittle materials. *Comput. Geotech.* **2015**, *65*, 126–135. [CrossRef]
35. Zhao, Z.; Yang, J.; Zhou, D.; Chen, Y. Experimental investigation on the wetting-induced weakening of sandstone joints. *Eng. Geol.* **2017**, *225*, 61–67. [CrossRef]
36. Hu, Y.; Deng, H.F.; Li, J.L.; Zhang, Y.C.; Wang, W.; Hu, Y.Y. Research on characteristics and mechanism of micro-structure variation in sandstone under water-rock interaction. *J. Disas Prev. Mitig. Eng.* **2018**, *38*, 265–281.
37. Brantut, N.; Heap, M.J.; Meredith, P.G.; Baud, P. Time-dependent cracking and brittle creep in crustal rocks: A review. *J. Struct. Geol.* **2013**, *52*, 17–43. [CrossRef]
38. Wang, Z.K.; Li, W.P.; Wang, Q.Q.; Liu, S.L.; Hu, Y.B.; Fan, K.F. Relationships between the petrographic, physical and mechanical characteristics of sedimentary rocks in Jurassic weakly cemented strata. *Environ. Earth Sci.* **2019**, *78*, 131. [CrossRef]
39. Zorlu, K.; Ulusay, R.; Ocakoglu, F.; Gokceoglu, C.; Sonmez, H. Predicting intact rock properties of selected sandstones using petrographic thin-section data. *Int. J. Rock Mech. Min.* **2004**, *41*, 93–98. [CrossRef]

Disclaimer/Publisher's Note: The statements, opinions and data contained in all publications are solely those of the individual author(s) and contributor(s) and not of MDPI and/or the editor(s). MDPI and/or the editor(s) disclaim responsibility for any injury to people or property resulting from any ideas, methods, instructions or products referred to in the content.